Journal of Applied Fluid Mechanics, Vol. 16, No. 8, pp. 1544-1559, 2023.
Available online at www.jafmonline.net, ISSN 1735-3572, EISSN 1735-3645.
https://doi.org/10.47176/jafm.16.08.1718

Assessment of Turbulence Models for Unsteady Separated Flows Past an Oscillating NACA 0015 Airfoil in Deep Stall

S. Ouchene[1†], A. Smaili[1] and H. Fellouah[2]

[1] *Laboratory of Green and Mechanical Development-LGMD, Ecole Nationale Polytechnique, B.P. 182, El-Harrach, Algiers, 16200, Algeria*
[2] *Department of mechanical engineering, Université de Sherbrooke, 2500 Boulevard de l'Université, Sherbrooke, Québec, J1K2R1 Canada*

†*Corresponding Author Email: samir.ouchene@g.enp.edu.dz*

ABSTRACT

This paper provides 2D Computational Fluid Dynamics (CFD) investigations, using OpenFOAM package, of the unsteady separated fully turbulent flows past a NACA 0015 airfoil undergoing sinusoidal pitching motion about its quarter-chord axis in deep stall regime at a reduced frequency of 0.1, a free stream Mach number of 0.278, and at a Reynolds number, based on the airfoil chord length, c, of 1.95×10^6. First, eighteen 2D steady-state computations coupled with the $k-\omega$ SST model were carried out at various angles of attack to investigate the static stall. Then, the 2D Unsteady Reynolds-Averaged Navier-Stokes (URANS) simulations of the flow around the oscillating airfoil about its quarter-chord axis were carried out. Three eddy viscosity turbulence models, namely the Spalart-Allmaras, Launder-Sharma $k-\varepsilon$, and $k-\omega$ SST were considered for turbulence closure. The results are compared with the experimental data where the boundary layer has been tripped at the airfoil's leading-edge. The findings suggest that the $k-\omega$ SST performs best among the other two models to predict the unsteady aerodynamic forces and the main flow features characteristic of the deep stall regime. The influence of moving the pitching axis downstream at mid chord was also investigated using URANS simulations coupled with the $k-\omega$ SST model. It was found that this induces higher peaks in the nose-down pitching moment and delays the stall onset. However, the qualitative behavior of the unsteady flow in post-stall remains unchanged. The details of the flow development associated with dynamic stall were discussed

Article History

Received December 15, 2022
Revised March 5, 2023
Accepted April 2, 2023
Available online May 31, 2023

Keywords:

Dynamic stall
Deep stall
Turbulence modeling
Numerical Simulation
Navier-Stokes Equations

1. INTRODUCTION

Dynamic stall is a phenomenon that affects airfoils or other lifting surfaces executing unsteady motion such as plunging, pitching or vertical translation that takes the angle of attack (AoA) beyond its static stall angle (Leishman, 2006). In contrast to static-stall behavior, dynamic stall is characterized primarily by delayed separation of the boundary layer to angles considerably exceeding the static stall angle, which produces higher lift values far in excess of their static counterparts. Afterward, a large vortical structure referred to as Dynamic Stall Vortex (DSV) is formed over the suction side of the airfoil. Convection and shedding of the DSV induce an abrupt loss in lift accompanied by a substantial increase in drag and a strong negative pitching moment with detrimental impacts on structural integrity and controllability (Visbal & Benton, 2018).

Dynamic stall is a performance-limiting phenomenon in a large variety of engineering applications, such as helicopter rotors and wind turbines (Ekaterinaris & Platzer, 1998; Geng et al., 2018). In particular, vertical axis wind turbines (VAWT) operating at low tip speed ratios which exhibit regularly dynamic stall due to the high amplitudes of AoAs perceived by the blades. Therefore, dynamic stall is intrinsic at their state of operation (Hand et al., 2021). Prediction of the flow in its complexity associated with dynamic stall is essential, not only to determine the average recovered power, but also to anticipate the cyclic loadings that induce material fatigue.

In the experimental investigations of airfoils undergoing sinusoidal pitching by Carr et al. (1977), three dynamic stall onset mechanisms have been identified: (a) trailing-edge separation that spreads gradually upstream and reaches the leading-edge, (b) abrupt turbulent se

Nomenclature

c	airfoil chord length	α	angle of attack
C_d	drag coefficient	α_1	oscillation amplitude
C_l	lift coefficient	α_m	mean angle of attack
C_m	pitching moment coefficient	ε	dissipation rate of turbulence kinetic energy
k	turbulence kinetic energy	κ	reduced frequency
Ma	Mach number	Ω	angular frequency of oscillation
Re_c	chord-based Reynolds number	ω	specific dissipation rate of turbulence kinetic energy
t	time		

paration near the leading-edge, and (c) bursting of leading-edge laminar separation bubble (LSB). Another mechanism discovered by McCroskey et al. (1981) involving a flow breakdown near a mid-chord location of initial boundary layer separation that progresses both downstream and upstream over the airfoil's suction side. The experiments were carried out for 2D airfoil sections under a wide range of unsteady flow conditions and parameters, including change of the airfoil leading-edge shape, Reynolds number, amplitude, and frequency of oscillation. It has been noted that despite the sensitivity of the stall onset mechanism to the parameters tested, no change in the qualitative behavior of dynamic stall as the airfoil penetrates in deep-stall regime. A large amount of subsequent experimental research has provided a great deal of information to improve the physical understanding of the parameters affecting the dynamic stall process, mainly stall onset. It became clear that this phenomenon is dependent on various interrelated parameters, including but not limited to: reduced frequency (Gharali et al., 2018; Thakor et al., 2020), Mach number (Sangwan et al., 2017), mean AoA, and amplitude of oscillation (Piziali, 1994; Lee & Gerontakos, 2004), type of motion (Lee & Su, 2015), freestream velocity profile (Gharali & Johnson, 2013), and Reynolds number (Gupta & Ansell, 2018). Despite the extensive experimental investigations that have been carried out and modeling of dynamic stall, this phenomenon is not fully understood. Particularly, the process leading to the formation of the primary vortex and mechanisms causing its detachment are still controversial (Wang & Xiao, 2020).

In the late 1970s, as the experimental investigations shed light on the basic physical aspects associated with dynamic stall, many researchers focused on developing semi-empirical engineering approaches to predict the stall behavior. The models differ by their complexity of modeling the elementary phenomena occurring during various stages of dynamic stall (Beaudet, 2014). Among these models, we can find: Onera model (Petot, 1989), Boeing-Vertol model (Tarzanin, 1972), and Leishman-Beddoes (Leishman & Beddoes, 1989). These models have been modified for wind turbine research and have seen widespread applications. Because these methods rely on experimental data to tune the model coefficients for specific airfoils, their application range is limited to conventional airfoil sections.

With the recent advances in computing power, computational methods, and turbulence modeling, the computation of the complex unsteady flows can be achieved using the full unsteady Navier-Stokes equations to overcome the limitations of the semi-empirical methods. However, choice of the turbulence model significantly affects the accuracy of these methods (Ekaterinaris & Platzer, 1998). Ko and McCroskey (1997) conducted a series of computations for the flow over an oscillating NACA 0015 airfoil in attached flow, light stall, and deep stall conditions with three turbulence models: the zero-equation Baldwin-Lomax, Spalart-Allmaras, and $k-\varepsilon$ turbulence models. Among the tested models, it was found that although the Spalart-Allmaras model performed best, none of these models were capable of predicting the deep stall case accurately, especially in the downstroke phase. In the late nineties, Ekaterinaris and Platzer (1998) have conducted a comprehensive review of Computational Fluid Dynamics (CFD) methods for dynamic stall and presented the major methods and the obtained results regarding dynamic stall prediction. The methods differ in the level of complexity, ranging from potential flow theory to Full-Navier-Stokes equations. Rhee (2007) carried out Unsteady Reynolds Averaged Navier-Stokes (URANS) computations of the flow over a NACA 0015 airfoil at fixed AoAs and in oscillating motion using the Spalart-Allmaras model for turbulence closure. The results revealed that the lift peak is highly overpredicted in quasi-steady cases, and the characteristics of the dynamic stall are poorly predicted as well. The modification of the turbulence model constant, C_{v1}, considerably improved the prediction of lift and the peak of the pitching moment, but the modification worsened the subsequent stall process in the dynamic case. Wang et al. (2010) investigated the flow around an oscillating NACA 0012 airfoil using the standard $k-\omega$ and the $k-\omega$ SST models at a moderate chord Reynolds number, $Re_c = 10^5$. They found that the $k-\omega$ SST performed best, but it was noticed that both models fail to predict the position and the size of the DSV accurately. Chitsomboon and Thamthae (2011) used the $k-\omega$ SST model with a damping function to limit the eddy viscosity in the buffer zone of the turbulent boundary layer to improve the flow separation prediction. Later, Bangga and Sasongko (2017) adopted this approach to adjust the eddy viscosity in the $k-\varepsilon$ model. Some improvements have been noticed compared to the standard model, but this adjusted model performed poorly in predicting the aerodynamic forces compared to the experimental data.

It should be highlighted that most studies of dynamic stall in the literature deal with relatively thin airfoil sections that have 12% thickness to chord length ratio (Refs. (Lee & Gerontakos, 2004; Spentzos et al., 2005; Wang et al., 2010; Belkheir et al., 2012; Wang et al., 2012;

Tseng & Cheng, 2015; Kim & Xie, 2016; Geng et al., 2018; Visbal & Garmann ,2018; Li et al., 2019; Surekha RS et al., 2019; Smith & Ventikos, 2019; Abbas et al., 2021)). (Sharma & Visbal, 2019) used large eddy simulations (LES) to investigate the effect of airfoil thickness on dynamic stall onset at $Re_c = 2 \times 10^5$. They found that the airfoil thickness changes the mechanism of stall onset from that triggered solely by the bursting of the LSB to that triggered by the interaction of the LSB with the trailing-edge separation. Coleman et al. (2019) used Parametric Modal Decomposition (PMD) of an airfoil pressure difference field to derive a reduced-order model (ROM) of dynamic stall phenomenon. In the light of results obtained for several operating conditions and airfoil geometries; it is conjectured that the ROM with two modes is sufficiently able to reconstruct the aerodynamic loads regardless of the dynamic stall regime and the airfoil geometry. However, the investigation is limited only to airfoils that exhibit leading-edge stall and the behavior of airfoils that exhibit other stall onset mechanisms is unknown.

To the best of authors knowledge, the relatively thicker airfoils, namely NACA 0015, was not thoroughly investigated, as opposed to relatively thinner airfoils such as NACA 0012, at severe stall conditions of deep stall. Yet, most of numerical studies that investigated dynamic stall used commercial software such as Ansys Fluent (Refs. Wang et al., 2012; Geng et al., 2018) or in-house codes (Refs. Rhee, 2007; Sharma & Visbal, 2019). The current work focuses on using only Open Source software, namely the OpenFOAM package (OpenCFD, 2022), to assess the ability of three commonly used URANS turbulence models, which are the Spalart-Allmaras, Launder Sharma $k-\varepsilon$, and $k-\omega$ SST models, to predict the complex unsteady flow of deep stall. The NACA 0015 airfoil is selected as the object of the present study undergoing a sinusoidal pitching motion around an axis located at its quarter-chord from the leading-edge, with a prescribed AoA, i.e., $\alpha(t) = 17 = 5\sin(\Omega t)$ at a reduced frequency, $\kappa = \Omega c/2U_\infty = 0.1$, where Ω is the oscillation frequency (Hz), and U_∞ is the free stream velocity (m/s). The freestream Reynolds number based on the airfoil chord is, $Re_c = 1.95 \times 10^6$, and the Mach number is $Ma = 0.278$. These conditions represent the most severe testing conditions of the NACA 0015 airfoil with a trip at the leading-edge from the experimental investigations of Piziali (1994) conducted in the 7-by 10 Foot subsonic wind tunnel at the NASA Ames Research Center. Several 2D RANS simulations coupled with the $k-\omega$ SST model have been conducted for various AoAs ranging from 0° to 18° to predict the static-stall under the same flow conditions. Additionally, this model has also been used to investigate the effect of displacing the pitching axis aft at mid-chord employing URANS computations. The results obtained by these computations, including the aerodynamic forces, pitching moment, vorticity contours, are presented and discussed. The contents of the paper are organized as follows. The methodology and test cases are introduced in Section 2. and Section 3. The results and validations are presented in Section 4. Finally, the conclusion is made in Section 5.

2. METHODOLOGY

2.1 Dynamic Mesh Handling

The sliding Mesh is a special case of dynamic mesh, where the cells and boundaries are moving in rigid-body motion, i.e., the distance between any two nodes remains constant over time, and hence the mesh cells are retaining their shape and volume. The mesh motion must be prescribed in such a way that the regions connected through conformal/ nonconformal sliding interfaces stay aligned with each other. The governing equations solved in these domains are inherently unsteady (Ansys, 2022). For dynamic mesh handling in the context of the finite volume method, the governing equation for a general scalar quantity ϕ is expressed in the integral form over an arbitrarily moving control volume $V(t)$ bounded by control surface $A(t)$. The equation is given by (Jasak, 2009; Ansys, 2022):

$$\frac{\partial}{\partial t}\int_V \rho\phi \, \mathrm{d}V + \oint_A \rho \mathbf{n}\cdot(\mathbf{u}-\mathbf{u}_g)\phi \, \mathrm{d}A = \oint_A \rho \, \Gamma_\phi \mathbf{n}\cdot\nabla\phi \, \mathrm{d}A + \int_V S_\phi \, \mathrm{d}V \tag{1}$$

Where ρ is the fluid density, $\mathbf{n}$ is an outwardly pointing unit normal vector on the boundary surface A, $\mathbf{u}_g$ is the mesh velocity, Γ_ϕ is the diffusion term, and S_ϕ is the source term of ϕ. The grid velocity $\mathbf{u}_g$ and the rate of change of volume V of the boundary surface A are related by the space conservation law:

$$\frac{\partial}{\partial t}\int_V \mathrm{d}V - \oint_A \mathbf{u}_g \cdot \mathbf{n} \, \mathrm{d}A \tag{2}$$

In the case of a sliding mesh motion, all the cells in the computational domain retain their initial volume, hence:

$$\oint_A \mathbf{u}_g \cdot \mathbf{n} \, \mathrm{d}A = 0. \tag{3}$$

2.2 Turbulence Models

Among the eddy viscosity turbulence models, the Spalart-Allmaras, $k-\omega$ SST, and $k-\varepsilon$ models are widely used (Rumsey, 2007; Spalart & Rumsey, 2007). Accordingly, in this study the Spalart-Allmaras, $k-\omega$ SST, and Launder Sharma $k-\varepsilon$ are selected. The common point between these models is that they are valid up to the wall, and thus no need for using wall functions. For the $k-\varepsilon$ model, the main motivation behind the choice of using the low-Re formulation is that wall functions require the first cell center of the computational grid to be placed in the log-layer region. However, in complex flows, where the mean quantities are highly time-dependent, this region does not necessarily exist (Jensen et al., 1989; Kaptein et al., 2020). Therefore, the use of wall functions for the $k-\varepsilon$ will likely be beyond its range of justifiability.

2.2.1 Spalart-Allmaras Model

The Spalart-Allmaras model solves a modeled transport equation for the kinematic eddy viscosity. It was originally developed for wall-bounded flows in aerospace applications (Spalart & Allmaras, 1992). The equation is given by (Catris & Aupoix, 2000):

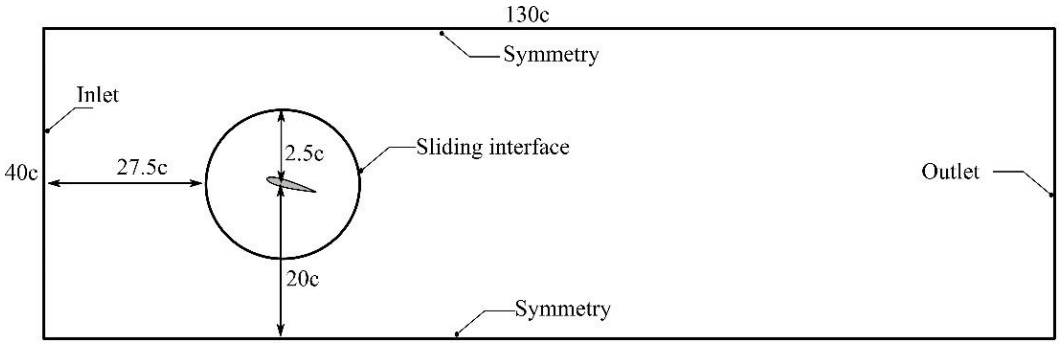

Fig. 1. Dimensions of the computational domain and boundary conditions.

$$\frac{\partial \rho\hat{\nu}}{\partial t} + u_j \frac{\partial \rho\hat{\nu}}{\partial x_j} = c_{b1}\hat{S}\rho\hat{\nu} - c_{w1} f_w \rho \left(\frac{\hat{\nu}}{d}\right)^2 + \\ + \frac{1}{\sigma}\frac{\partial}{\partial x_j}\left(\mu \frac{\partial \hat{\nu}}{\partial x_j}\right) + \frac{1}{\sigma}\frac{\partial}{\partial x_j}\left(\sqrt{\rho}\hat{\nu}\frac{\partial \sqrt{\rho}\hat{\nu}}{\partial x_j}\right) + \\ + \frac{c_{b2}}{\sigma}\frac{\partial \sqrt{\rho}\hat{\nu}}{\partial x_i}\frac{\partial \sqrt{\rho}\hat{\nu}}{\partial x_i} \tag{4}$$

2.2.2 Launder Sharma $k-\varepsilon$ Model

In literature, there are many common Low-Re formulations of the $k-\varepsilon$ model. In this study, the Launder Sharma formulation is considered (Launder & Sharma, 1974; Tahry, 1983). The Low-Re formulation of the standard $k-\varepsilon$ is achieved by damping the model coefficients close to the wall by applying damping functions: f_2, and f_μ to C_1 and C_μ coefficients, respectively:

$$\widehat{C_2} = f_2 C_2, \tag{5}$$

$$\widehat{C_\mu} = f_\mu C_\mu. \tag{6}$$

Where $f_2 = 1 - 0.3\exp[-(k^2/50\nu\varepsilon)^2]$, and $f_\mu = \exp[-3.4/(1+k^2/50\nu\varepsilon)]$.

OpenFOAM uses the most up-to-date coefficients of the $k-\varepsilon$ model from Ref. (Launder & Sharma, 1974) with $C_1 = 1.44$, $C_2 = 1.92$, $\sigma_k = 1$, $\sigma_\varepsilon = 1.3$, and $C_\mu = 0.09$.

2.2.3 $k-\omega$ SST Model

The $k-\omega$ SST model, introduced by Menter (1994), combines the $k-\varepsilon$ model and the Wilcox $k-\omega$ model through a blending function in addition to a viscosity limiter. The blending function switches to the Wilcox $k-\omega$ model near the walls and the $k-\varepsilon$ in the free stream. The Wilcox $k-\omega$ is a low Re turbulence model that is usable all the way down to the wall through the viscous sublayer. It has been shown to give good results in boundary layers subjected to adverse pressure gradients and mildly separated flows that cannot be predicted accurately by the $k-\varepsilon$ model but has a strong sensitivity to free stream value of ω at the inlet (Geng et al., 2018). The $k-\omega$ SST model attempts to address these issues by combining the benefits and mitigating the shortcomings of the two models. OpenFOAM implementation of $k-\omega$ SST is based on the 2003 model (Menter et al., 2003):

$$\frac{\partial \rho k}{\partial t} + \frac{\rho U_i k}{\partial x_i} = \widetilde{P_k} - \beta^* \rho k\omega + \\ + \frac{\partial}{\partial x_i}\left((\mu + \sigma_k \mu_t)\frac{\partial k}{\partial x_i}\right) \tag{7}$$

$$\frac{\partial \rho\omega}{\partial t} + \frac{\rho U_i \omega}{\partial x_i} = \alpha\rho S^2 - \beta\rho\omega^2 + \\ + \frac{\partial}{\partial x_i}\left((\mu + \sigma_\omega \mu_t)\frac{\partial \omega}{\partial x_i}\right) + \\ + 2(1-F_1)\rho\sigma_{\omega 2}\frac{1}{\omega}\frac{\partial k}{\partial x_i}\frac{\partial \omega}{\partial x_i} \tag{8}$$

With the following model constants:

$\alpha_1 = 5/9$, $\beta^* = 0.09$, $\beta_2 = 0.0828$, $\beta_1 = 3/40$, $\sigma_{k1} = 0.85$, $\sigma_{\omega 1} = 0.5$, $\alpha_2 = 0.44$, $\sigma_{k2} = 1$, $\sigma_{\omega 2} = 0.856$.

3. COMPUTATIONAL DOMAIN AND GRID

3.1 Dynamic Case

The 2D computational domain for the unsteady simulations consists of two regions, as shown in Fig. 1. The oscillating circular region has a radius of $2.5c$ and is connected to the stationary rectangular region through a sliding interface. In OpenFOAM, this is achieved using the Arbitrary Mesh Interface (AMI) technique. The width and the length of the computational domain are set to $40c$, and $130c$ respectively. The distance from the leading-edge of the airfoil to the inlet is $30c$, while the outlet is located at $100c$ downstream. The distances of top and bottom boundaries were set to $20c$ from the center of the oscillating region. The distances are sufficiently high to avoid nonphysical effects of the boundaries being too close to the airfoil and allowing the wake flow to fully develop downstream the airfoil. To ensure a high-quality grid for the URANS computations, particularly in the oscillating region, much care was taken for mesh generation: Both hyperbolic and elliptic approaches combined with RBF (Radial Basis Functions) were used. First, the grid around the airfoil was generated via hyperbolic marching. This approach has several advantages; it is one to two orders of magnitude faster than the elliptic approach and generates nearly orthogonal grids (Chan & Steger, 1992).

However, the outer boundary cannot be specified precisely to get a perfect circular region, required by the sliding mesh approach in this case. To overcome this limitation, Radial Basis Functions (Bos et al., 2013) were used to morph the grid to a perfect circular region. Finally,

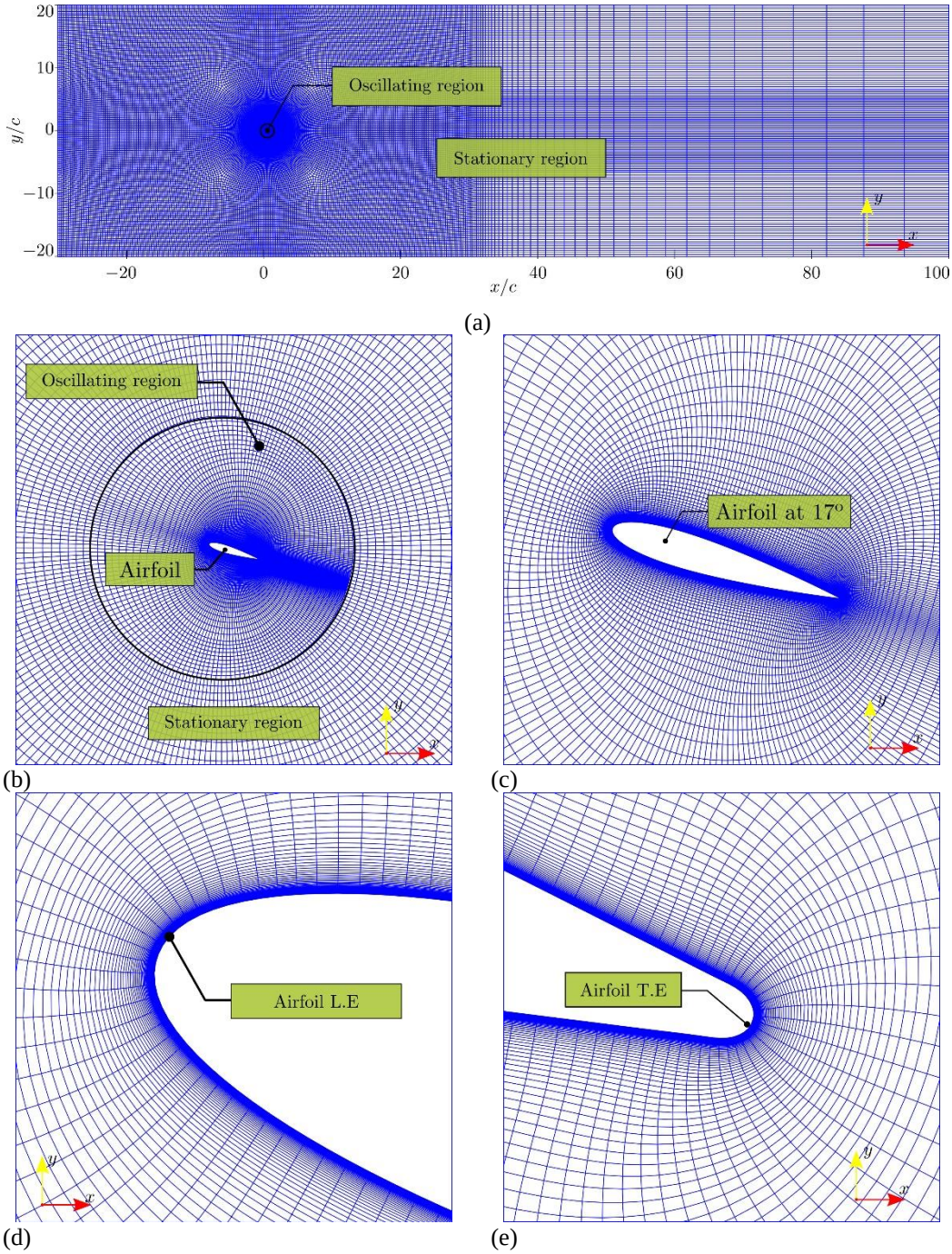

Fig. 2. Computational grid used for dynamic stall case. The same grid is used for the static cases but with a fixed domain, (a): the dimensions of the computational domain. (b): detailed grid around the oscillating region. (c): grid around the airfoil. (d): close up view of the grid near the leading-edge. (e): close-up view of the grid around the trailing-edge of the airfoil.

the grid was run through an in-house elliptic solver implemented in Python programming language to enhance its quality.

In the reference grid, 500 grid points were placed along the surface of the airfoil and clustered at the leading and the trailing edges. The height of the first cell layer in the normal direction to the wall was set to $5.65 \times 10^{-6}c$ to adequately resolve the boundary layer and ensuring a y^+ less than unity. The growth rate of cells normal to the airfoil surface is set to 1.1. The reference grid is shown in Fig. 2a with close-up views of the oscillating region (Fig. 2b), the grid around the airfoil (Fig. 2c), and near the leading-edge of the airfoil (Fig. 2d). A rounded trailing-edge is used, as depicted in Fig. 2e.

3.1.1 Boundary Conditions

In accordance with the 2D experiments of Piziali (1994), the airfoil employed in the current URANS computations is a NACA 0015 airfoil with a chord length of $c = 0.3048\,m$. The airfoil is undergoing a sinusoidal pitching motion about an axis located at a quarter-chord ($x/c = 25\%$) from its leadingedge with a mean angle of attack, α_m of 17°, i.e., $\alpha(t) = 17 + 5\sin(\Omega t)$ and a

Table 1 The values of the parameters used in the dynamic stall simulations (Piziali, 1994).

Airfoil	NACA 0015
Airfoil chord length, c	0.3048 m
Mean angle of attack, α_m	17°
Oscillation amplitude, α_1	5°
Angular frequency, Ω	20 π rad/s
Reduced Frequency, κ	0.1
Reynolds number, Re_c	1.95×10^6
Mach number, Ma	0.278

reduced frequency of 0.1. The reduced frequency is a prominent factor determining the degree of unsteadiness of the problem (Leishman, 2006). It is defined as $\kappa = \Omega c/2U_\infty$, where U_∞ is the freestream velocity and Ω is the oscillation frequency. At the inlet, the freestream Mach number is $Ma = 0.278$, and the Reynolds number, $Re_c = 1.95 \times 10^6$, based on the airfoil chord length, c. The freestream turbulence intensity was not reported in the experiment. Nevertheless, according to Storms et al. (2001), the longitudinal turbulence level in the NASA Ames 7-by 10-ft wind tunnel is 0.1% for an empty test section and 0.25% at $Ma = 0.22$. Thereby, a value of $TI = 0.25\%$ is used in the present study. These parameters are summarized in Table 1. A symmetry boundary condition is imposed assuming a zero gradient of flow quantities and a parallel flow at the bottom and top of the computational domain. At the airfoil surface, a no-slip boundary condition is imposed. The motion of the circular zone containing the airfoil is prescribed to follow a sinusoidal pattern through the *oscillatingRotatingMotion* function in OpenFOAM (OpenCFD, 2022). A similar setup is used for the unsteady simulation involving the same NACA 0015 airfoil executing an oscillation about a mid-chord axis.

3.2 Static Case

In the current investigation of the static-stall prediction, 2D steady RANS were performed for the computation of the flow past a NACA 0015 airfoil over a range of AoAs between 0° to 18° in increment of 1°, at a Reynolds number based on the airfoil chord-length of $Re_c = 1.95 \times 10^6$ and $Ma = 0.278$. The results are compared with the experimental data reported by Piziali (1994). These measurements were conducted for a NACA 0015 airfoil with a tripped boundary layer at the leading-edge pitching at such a low reduced frequency that the resulting stall can be considered a static stall. Apart from using a computational domain with a static grid at each AoA, the same computational domain and the numerical setup used in the dynamic case (as described above) are used for the steady-state simulations.

3.3 Numerical Procedure

The governing equations of the flow (Eq. 1) in the form of 2D compressible URANS equations coupled with the aforementioned turbulence models, discretized based on the finite volume method, are numerically integrated using OpenFOAM (OpenCFD, 2022). *rhoSimpleFoam* and

Table 2 Properties of the grids used for grid convergence study. y_1 is the height of the first cell layer, N_{pts}: Number of points on the airfoil surface.

Grid	y_1	Growth rate	N_{pts}	No. cells
Grid 1	1.13×10^{-5} c	1.1	250	124866
Grid 2	8.00×10^{-6} c	1.1	354	187650
Grid 3	5.65×10^{-6} c	1.1	500	296748
Grid 4	4.00×10^{-6} c	1.1	708	478476

rhoPimpleFoam solvers are used for steady-state and the unsteady simulations, involving dynamic mesh, respectively. The PIMPLE algorithm, which is a combination of PISO and SIMPLE algorithms (Greenshields & Weller, 2022), is used for pressure-velocity-energy coupling. All the unsteady computations were started using first-order schemes for the first few time steps to ensure the stability of the solution, and then second-order accurate schemes were used for the temporal term and spatial discretizations of convection and diffusion terms. The time step was adjusted automatically based on the maximum courant number of $|U|\delta x/\delta t = 0.6$. This value is selected based on analysis of time step sensitivity by using the following values for the maximum courant number: 0.5, 0.6, and 0.7. No significant changes happened from 0.5 to 0.6, so the value of 0.6 is selected for all the computations. The simulations were performed with 92 AMD Opteron™ 6174 2.2 GHz cores on Mammouth Parallèle II cluster of Compute Canada's network.

3.4 Grid Convergence Study and Convergence of Simulations

In order to perform a grid convergence analysis of the unsteady simulations, a total of four grids were generated with the same topology and dimensions of the computational domain, Grid 1 to Grid 4 (See Table 2). The number of grid cells is changed by a factor of $\sqrt{2}$ in both normal and streamwise directions. In addition to the reference grid (Grid 3) with 296748 cells, this results in three grids: Grid 1, Grid 2, and Grid 4 with 124866 cells, 187650 cells, and 478476 cells, respectively. The growth rate of the cells expanding from the airfoil surface remains unchanged. Table 2 lists the properties of these grids.

Figure 3 presents the ensemble-averaged lift coefficient, C_l, hysteresis loops over the last 5 cycles, obtained using URANS computations with $k-\omega$ SST employing the four grids, Grid 1 to Grid 4, and are compared with the experimental results of Piziali (1994). It can be seen that C_l prediction using Grid 1 differs from the other three grids in the upstroke and downstroke phases of the pitching cycle. Moreover, the results of Grid 1 and Grid 2 substantially differ from the results of Grid 3 and Grid 4 in the post-stall regime during the downstroke phase. However, during the upstroke phase, the predictions using all three grids, Grids 2-4, follow the same trend and C_l values are almost identical. By examining the flow field details obtained by both Grid 3 and Grid 4, no noticeable differences are observed even though minor discrepancies are observed in the lift

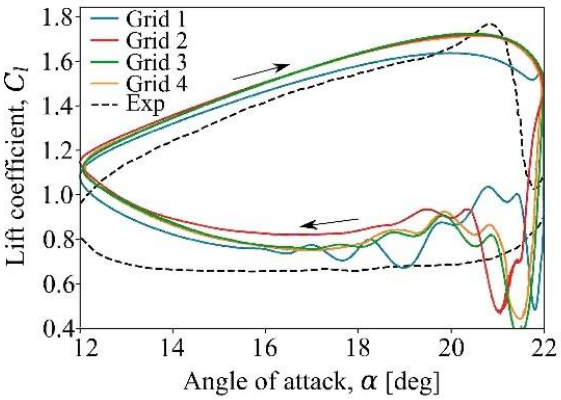

Fig. 3. Comparison of the lift coefficient predicted by the different grid densities using the $k-\omega$ SST model.

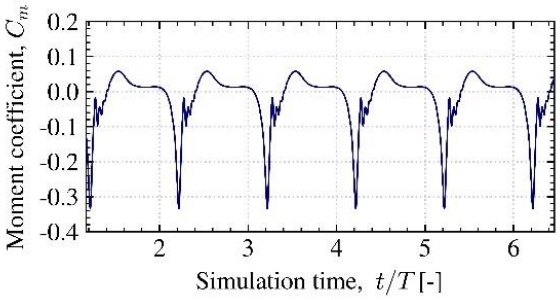

Fig. 4. Variation of pitching moment coefficient as a function of dimensionless time, t/T for the reference case (Grid 3) using $k-\omega$ SST model.

coefficient immediately after the stall. These discrepancies are due to the complex unsteady behavior of the flow during the post-stall process (Ekaterinaris & Platzer, 1998). As the AoA decreases, the difference in C_l obtained by Grid 3 and Grid 4 is much smaller. Hence, a grid-independent solution is deemed to be achieved using Grid 3 as it presents a trade-off between computational cost and accuracy. The subsequent simulations with the SA and LS $k-\varepsilon$ models are based on Grid 3 as well.

The time history of the moment coefficient, C_m, is depicted in Fig. 4. In order to statistically assess the convergence of the simulations, the standard deviation of the aerodynamic coefficients, C_l, and C_m, between two successive pitching cycles are reported in Table 3. A difference in the aerodynamic coefficients between the first and the second pitching cycles is noticed, but this difference is negligible between the rest of the cycles starting from the second cycle. This suggests that a statistically steady solution is obtained. Therefore, the aerodynamic coefficients are ensemble-averaged over this time range of 5 cycle periods with $T = 2\pi/\Omega$, the cycle period. The aerodynamic coefficients predicted by the URANS simulations in the deep stall case were compared with the experimental dataset Piziali (1994), in which 20 cycles of data were acquired and ensemble-averaged.

Table 3 Standard deviations of differences of pitching moment and lift coefficients between consecutive pitching cycles.

Std. deviation, σ (%)	σ_1	σ_2	σ_3	σ_4	σ_5	σ_6
Moment coefficient	4.32	0.01	0.01	0.00	0.00	0.00
Lift coefficient	6.17	0.02	0.011	0.011	0.01	0.01

4. Results and Discussion

4.1 Static Case

The objective of the current section is to determine the static stall AoA. For this reason, 2D steady-state RANS computations are conducted employing the $k-\omega$ SST turbulence model as it performs better among other models for the static case (Suvanjumrat, 2017). Shown in Fig. 5 are the obtained results: the lift coefficient (a), drag coefficient (b), and pitching moment coefficient (c) as a function of angle of attack, α .

The results are compared with the quasi-steady measurements reported by Piziali (1994). It's worth noting that the quasi-steady measurements are conducted at a low frequency, $\Omega \leq 0.04$ Hz such that the resulting stall is considered as a static stall. In Figs. 5a to 5c, only the upstroke part of the experimental dataset is plotted. For.

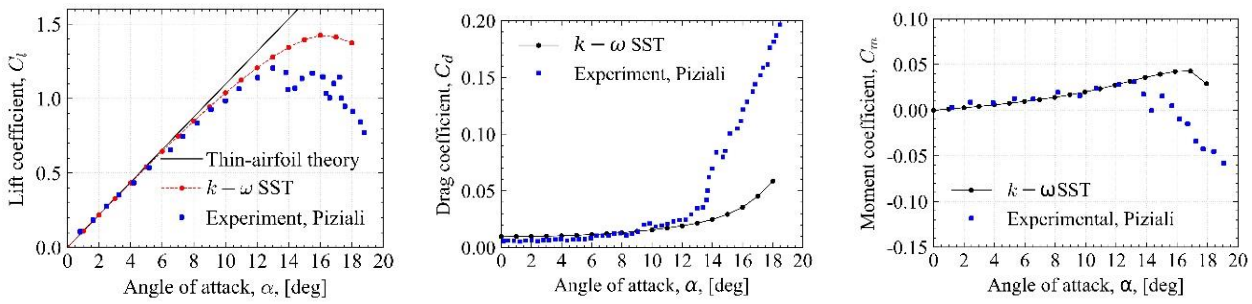

(a) (b) (c)

Fig. 5. The aerodynamic coefficients as functions of angle of attack: (a): lift coefficient, (b): drag coefficient, and (c): pitching moment coefficient of a NACA 0015 airfoil, at a Reynolds number of $Re_c = 1.95 \times 10^6$. Computed using $k-\omega$ SST model. Results are compared with the experimental measurements of Piziali (1994).

low AoAs, namely, $\alpha \leq 8°$, the lift coefficient, C_l, is reasonably close to the experimental data. Both curves follow a linear trend with a slope, $dC_l/d\alpha \approx \pi^2/90$ as predicted by the thin airfoil theory. However, for higher AoAs, the $k-\omega$ SST model starts to overpredict C_l as the AoA increases progressively. The deviation of the C_l curve from the linear behavior is due to the increase of the boundary layer thickness on the suction surface of the airfoil caused by the adverse pressure gradients (Leishman, 2006). The difference between the two curves becomes much more noticeable for $\alpha > 13°$. In fact, the static stall has already occurred at $\alpha \approx 13°$, ($C_{l,max} \approx 1.2$), whereas the model predicts a higher static stall around $\alpha \approx 16°$ ($C_{l,max} \approx 1.42$. This disagreement is attributed to the delayed prediction of the turbulent boundary layer separation on the airfoil's upper surface under adverse pressure gradients (Wang & Xiao, 2020). The overprediction of the lift coefficient and the underestimation of drag coefficient near the static stall using the $k-\omega$ SST model was also reported by Wang and Xiao (2020) even with a tripped airfoil. Variation of the drag coefficient with the increase in AoA is shown in Fig. 5b. In the range of $0° \leq \alpha \leq 9°$, the drag coefficient computed using the $k-\omega$ SST model is slightly higher than the experimental values, although the trend of the two curves is in good agreement. This overprediction of drag is likely because the viscous wall shear stress contribution was not included in the measured forces. Hence, the aerodynamic coefficients were integrated from pressure data only. For larger AoAs, namely, $\alpha > 9°$, C_d values are underestimated, and the difference becomes much more prominent for AoAs exceeding the static stall angle ($\alpha \approx 13°$). The quarter-chord pitching moment (Fig. 5c) is reasonably well predicted for AoAs below static stall angle ($\alpha_{ss} \approx 13°$). However, past stall angle, the C_m values are overpredicted, resulting in a delay in stall. It is worth noting that in this case, the $k-\omega$ SST model predicts a positive pitching moment coefficient over the range of AoAs, implying that the pressure center is ahead of the quarter chord point.

4.2 Dynamic Stall Cases

4.2.1 Aerodynamic coefficients

This section presents the aerodynamic coefficients obtained from the 2D URANS of the flow around the oscillating airfoil about its quarter-chord axis using the three turbulence models: $k-\omega$ SST, Spalart-Allmaras, and LS $k-\varepsilon$. The experimental data of Piziali (1994) are included for comparison. It is worth noting that the subsequent analysis of the results follows the nomenclature set by McCroskey (1981), who classified the dynamic stall into four categories:

1. *No-stall*: In this regime, the AoA does not exceed the static stall angle, α_{ss}. A linear response is observed in the aerodynamic loads with slight hysteresis, but with no negative nose-down pitching moment.
2. *Stall onset*: In this regime, the AoA reaches the static stall angle. Under these conditions, the maximum useful lift is produced without excessive drag or pitching moment.
3. *Light stall*: Or moderate stall, in which a mild hysteresis in aerodynamic loads is observed with a less severe increase in drag and generation of negative nose-down pitching moment.
4. *Deep stall*: In this regime, severe hysteresis loops with significant peaks are observed in the aerodynamic loads. A pitching moment coefficient as much as 0.15 or beyond is considered to constitute a deep stall case.

Figures 6a to 6c show the lift coefficient's hysteresis loops predicted by $k-\omega$ SST (a), Spalart-Allmaras (b), and LS $k-\varepsilon$ (c) turbulence models respectively. For readability's sake and as not to encumber the graphs, the aerodynamic coefficients are plotted separately together with the experimental data. It can be seen that the $k-\omega$ SST model (Fig. 6a) overpredicts the lift coefficient during the upstroke cycle. However, its slope is in good agreement with the experimental data, even for higher AoAs up to $\alpha \approx 19.60° \uparrow$. However, the stall angle lagged the measured value by approximately 1°, and the predicted $C_{l,max} = 1.72$ (at $\alpha \approx 20.4° \uparrow$) is 2.8% smaller than the experimental value, which is about 1.77. On the other hand, the SA model (Fig. 6b) tends to underpredict C_l for increasing AoAs. Moreover, the predicted $C_{l,max} = 1.486$ is 16% less than the experimental $C_{l,max}$. The LS $k-\varepsilon$ model (Fig. 6c) predicts a $C_{l,max}$ (at $\alpha \approx 20.75° \uparrow$) nearly identical to the experimental value. Still, the C_l curve's overprediction is relatively high compared to $k-\omega$ SST during the upstroke cycle. During the downstroke motion, the C_l curve computed with $k-\omega$ SST exhibits a substantial drop shortly after the stall ($\alpha \approx 22°$). It shows an oscillatory behavior with the lowest value, $C_{l,min} \approx 0.36$ (at $\alpha \approx 21.45° \downarrow$). Geng et al. (2018), Wang et al. (2012), and Tseng and Cheng (2015) have also reported this behavior. This discrepancy is attributed to the complex flow features in the post-stall region characterized by vortex shedding, as illustrated below by vorticity contours (Fig. 8). The C_l curve increases rapidly for AoAs below the static stall, $\alpha_{ss} \approx 16°$ (as predicted by static computations) to recover the linear behavior. In contrast, the SA model highly overpredicts the C_l curve during the downstroke phase ($C_{l,min} \approx 0.91$ at $\alpha \approx 18.48° \downarrow$), and the C_l curve remains approximately constant for a large portion of the downstroke phase; AoAs down to $\alpha \approx 16°$. The LS $k-\varepsilon$ model significantly overpredicts the C_l curve during this phase, even higher than the SA model. It reaches only a $C_{l,min}$ of 1.12 (at $\alpha \approx 18.11° \downarrow$), that is, 39% higher than the experimental value ($C_{l,min} \approx 0.65$, at $\alpha \approx 15.67° \downarrow$). It should be noted that both SA and LS $k-\varepsilon$ models predicted narrow and smooth loops for the lift coefficient that lack the abruptness observed in the C_l hysteresis loop computed by the $k-\omega$ SST model. This observation also extends to the drag and pitching moment coefficients.

The drag coefficients are depicted in Figs. 6d to 6f. The value of C_d obtained by the $k-\omega$ SST model is in good agreement with the experimental data for AoAs below the static stall angle, $\alpha \approx 16°$. However, it tends to underestimate the C_d for higher AoAs. The drag value near

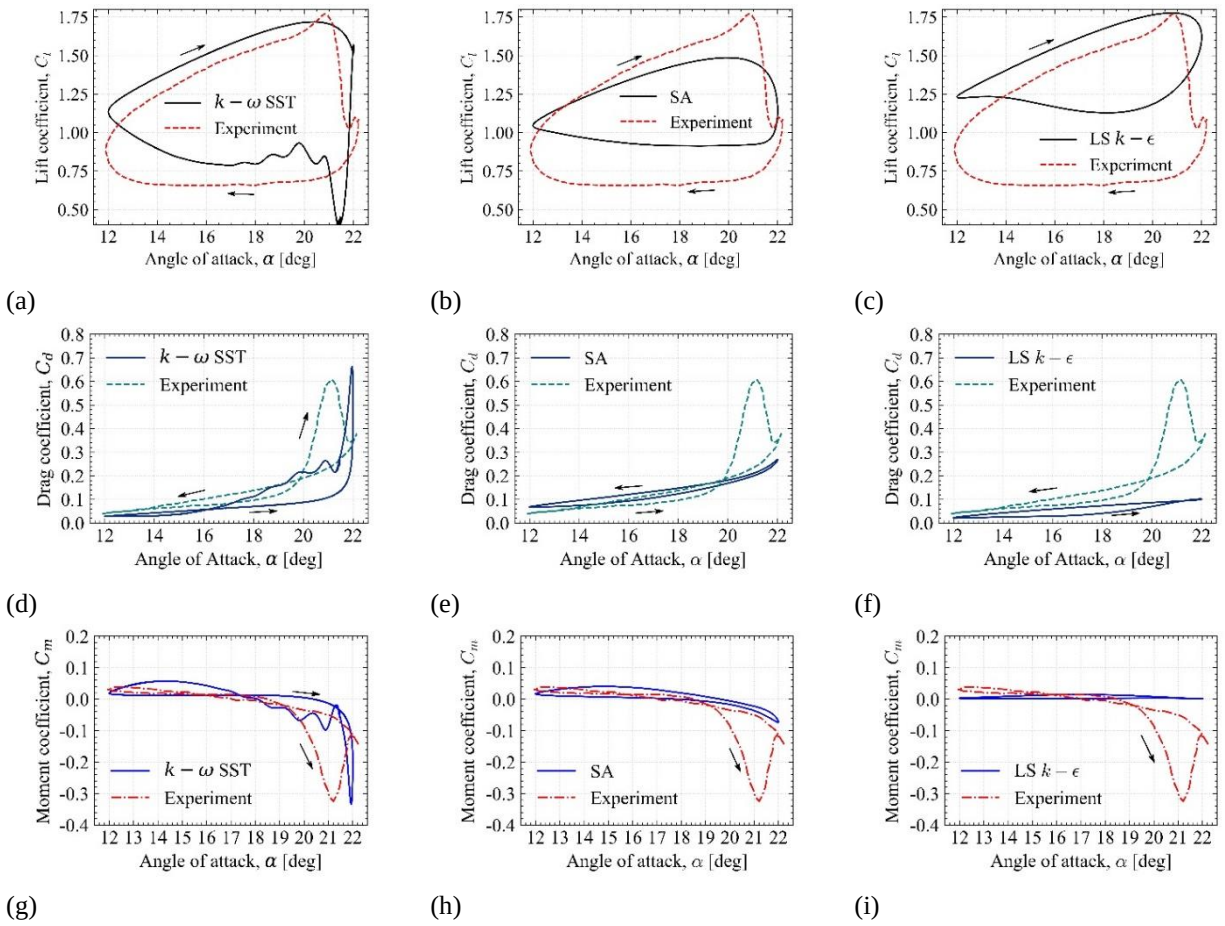

Fig. 6. Lift, drag, and pitching moment coefficients of a NACA 0015 airfoil as a function of angle of attack, at a Reynolds number of $Re_c = 1.95 \times 10^6$. (a-c): Lift coefficient computed using $k-\omega$ SST, SA, and LS $k-\epsilon$ models, respectively. (d-f): Drag coefficient computed using $k-\omega$ SST, SA, and LS $k-\epsilon$ models, respectively. (g-i): Pitching moment coefficient computed using $k-\omega$ SST, SA, and LS $k-\epsilon$ models, respectively. Results are compared with the experimental measurements of Piziali (1994).

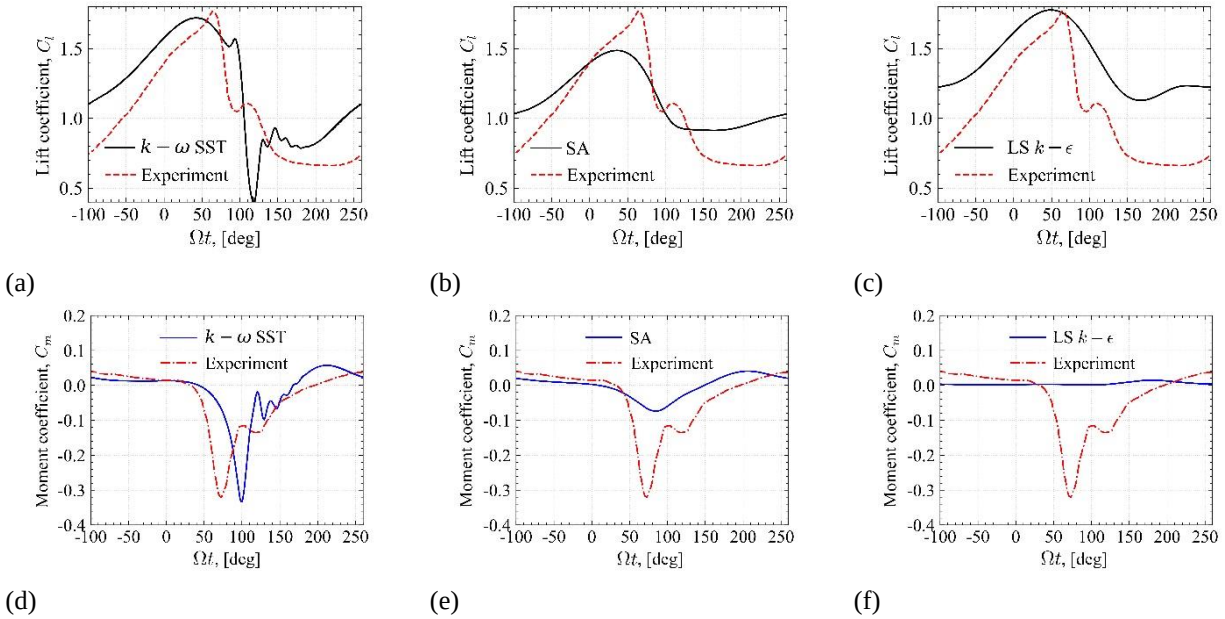

Fig. 7. Lift and pitching moment coefficients plotted as functions of the phase angle for the case of an airfoil oscillating about quarter-chord for different turbulence models: (a-c): Lift coefficient computed using $k-\omega$ SST, SA, and LS $k-\epsilon$ models and (d-f): pitching moment coefficient computed using $k-\omega$ SST, SA, and LS $k-\epsilon$ models, respectively. Results are compared with the experimental data (Piziali, 1994).

stall is relatively well predicted ($C_{d,max} \approx 0.66$ at $\alpha \approx 1.95°$) compared to the experimental value ($C_{d,max} \approx 0.6$, at $\alpha \approx 21.15° \uparrow$); hence the computed drag peak lags the experimental value by 0.8°. The C_d obtained by the SA model in Fig 6. (e) appears to follow the experimental C_d curve during the upstroke phase for AoAs up to $\alpha = 20° \uparrow$ but fails to predict the $C_{d,max}$. In fact, the C_d curve is nearly overlapping during both the upstroke and downstroke phases. Similar behavior is also observed in the C_d curve obtained by the LS $k-\varepsilon$ model (Fig. 6f), but with much smaller drag values. Shown in Figs. 6g and 6i are the pitching moment coefficients obtained employing the three turbulence models. For low AoAs below $16° \uparrow$ during the upstroke phase, the C_m obtained by $k-\omega$ SST (Fig. 6g) correlates well with experimentally measured C_m. The computed peak value of the nose-down pitching moment is around -0.33, which is close to the measured value of -0.32. The LS $k-\varepsilon$ model fails noticeably to reproduce the measured C_m loop. Actually, the computed C_m curve is positive during the entire upstroke phase ($C_{m,min} = 0.001$, at $\alpha \approx 21.91° \uparrow$). The SA model presents a slightly better prediction than LS $k-\varepsilon$, but still, the overshoot in the nose-down pitching moment was not captured. The lowest computed C_m value is only -0.07 (at $\alpha \approx 21.97° \uparrow$).

It becomes apparent that both the computed aerodynamic forces and the quarter-chord pitching moment using the LS $k-\varepsilon$ and the SA models noticeably lack the abruptness near the stall angle characteristic of a deep stall case. Remarkably, the LS $k-\varepsilon$ results suggest that the airfoil exhibits only "stall onset". In contrast, the SA model indicates that the airfoil experiences a "moderate stall" since the maximum magnitude of the predicted nose-down pitching moment doesn't exceed 0.15 (Rhee, 2002). The lift and pitching moment coefficients obtained from the unsteady simulations employing the URANS turbulence models are plotted as functions of the phase angle, Ωt, (Figs. 7a to 7f). In the case of $k-\omega$ SST model, the pitching moment coefficient (Fig. 7d) abruptly drops in the range of $50° < \Omega t < 100°$, whereas the lift coefficient changes in the range $100° < \Omega t < 150°$. This lag between lift and pitching moment coefficient indicates that the center of pressure position on the suction surface, has moved and the airfoil exhibits moment-stall before the occurrence of lift stall. The SA model predicts a change in the pitching moment coefficient (Fig. 7e) in the range of $20° < \Omega t < 80°$, while the lift coefficient changes in the range of $40° < \Omega t < 110°$ indicating a movement of the center of pressure before the drop in lift. However, as discussed above, the change in the pitching moment coefficient is mild compared to the $k-\omega$ SST case. In contrast to the previous two cases, the pitching moment coefficient curve computed using LS $k-\varepsilon$ model (Fig. 7f), shows an insignificant change in the range of $100° < \Omega t < 120°$ whereas the change in the lift after reaching its peak is in the range of $50° < \Omega t < 110°$. This behavior indicates that the flow separation is not sufficiently large on the suction side of the airfoil to affect the center of pressure position. It is likely attributed to the model being too diffusive and hence fails to predict the adverse pressure gradients in the turbulent boundary layer near the trailing-edge region.

4.2.2 Dynamic Stall Process

The unsteady flow predicted by the unsteady simulations employing URANS turbulence models is illustrated by visualizing the spanwise component of the vorticity field. The vorticity contours are presented at several characteristic AoAs, during the full oscillation cycle, that mark the main flow features associated with the dynamic stall exhibited by the oscillating NACA 0015 airfoil about its quarter-chord axis. Figure 8 shows the spanwise component of the vorticity together with the corresponding streamlines obtained employing the three turbulence models: $k-\omega$ SST, Spalart-Allmaras (SA), and the LS $k-\varepsilon$.

4.2.3 The $k-\omega$ SST Model

As shown in spanwise vorticity contours computed with the $k-\omega$ SST model (Fig. 8a), in the early stages of the pitch-up motion, namely $12° \leq \alpha \leq 16.5°$, the flow remains fully attached to the airfoil's upper surface. As the AoA continues to increase, the turbulent boundary layer separation spreads gradually toward the leading-edge and takes place over the entire suction surface of the airfoil. The separated shear layer rolls up and grows into a DSV, and in response, a secondary counterclockwise vortex forms near the trailing-edge. The DSV gains its maximum size and intensity at $\alpha \approx 22°$. During its period of residence over the airfoil, it induces an additional lift, as can be seen in Fig. 7a. The shedding of the primary trailing-edge vortex (TEV) into the wake causes a drop in the lift curve and a large overshoot in the nose-down pitching moment coefficient. During the downstroke stage, the flow is fully separated on the airfoil's upper surface. It is characterized by vortex shedding that cause the oscillation in the aerodynamic forces (see Fig. 6a and Fig. 6d) and the pitching moment coefficient (Fig. 6g). Additionally, the flow looks more complex on the airfoil suction surface, particularly near the leading-edge with the emergence of a pair of two contra-rotating vortices (see, $\alpha \approx 21.4° \downarrow$). As the airfoil continues to pitch down, the boundary layer starts to reattach from the leadingedge to the trailing-edge. This process is slow, as can be seen at $\alpha \approx 14.32° \downarrow$ where the turbulent boundary layer is still not fully attached. It should be noted that the series of stall events computed by the $k-\omega$ SST model indicate that the NACA 0015 airfoil exhibits a trailing-edge stall instead of a leading-edge stall. These predictions are in alignment with the conclusions of Rhee (2002, 2007). The trailing-edge stall category is generally associated with relatively thick airfoil sections (Sharma & Visbal, 2019), Whereas thin airfoils exhibit leading-edge dynamic stall, which is usually associated with the bursting of a laminar separation bubble near the leading-edge (Sharma & Visbal, 2019).

4.2.4 The Spalart-Allmaras Model

Figure 8b depicts the spanwise component of the vorticity as predicted by the Spalart Allmaras model. During the upstroke motion of the airfoil, the flow can be considered as non-separated for AoAs up to $\alpha < 18.75° \uparrow$.

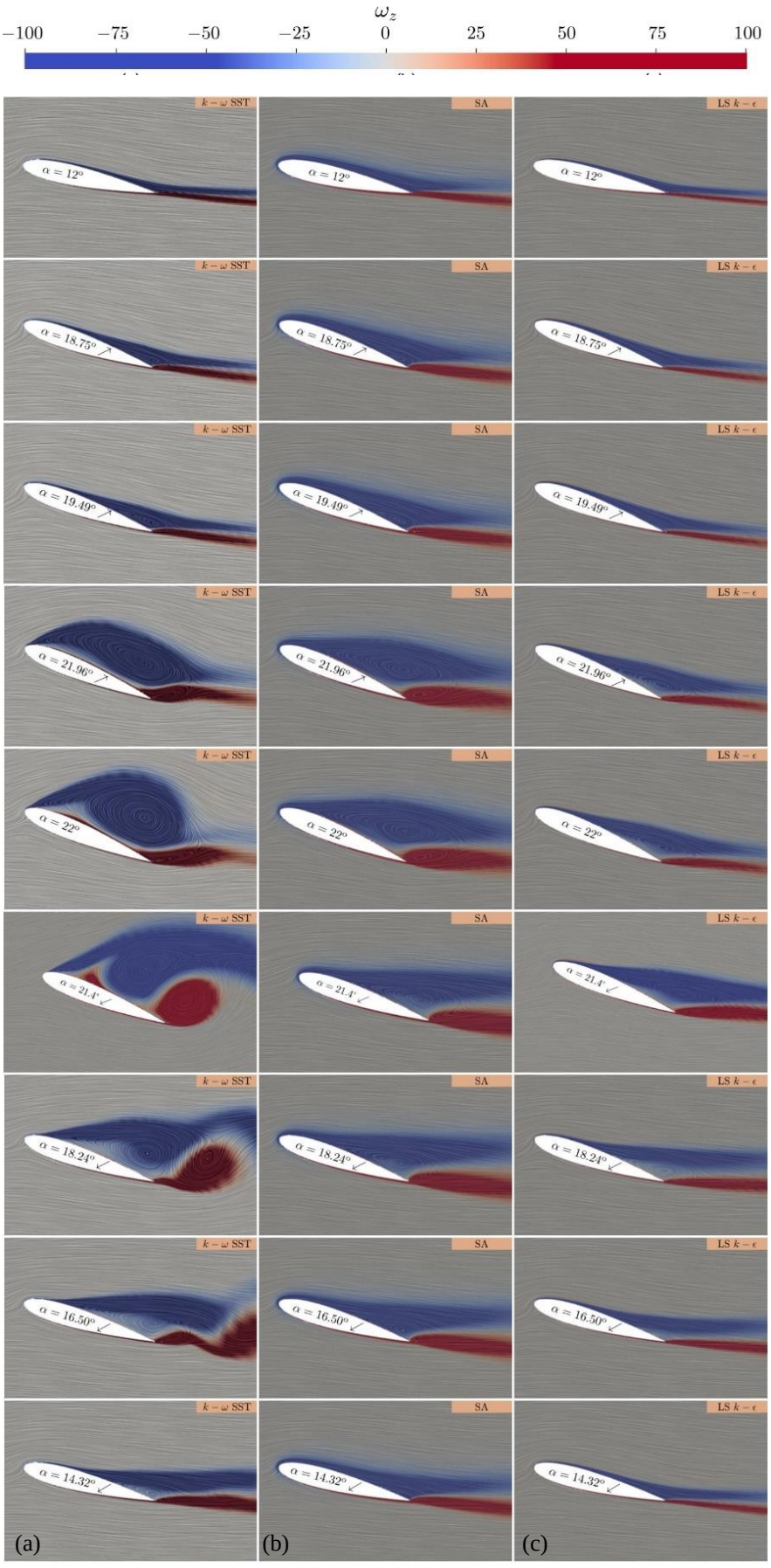

Fig. 8. Vorticity contours for the oscillating airfoil, $\alpha(t) = 17 + 5\ \sin(\Omega t)$ with $\kappa = 0.1$, about $x/c = 25\%$ axis, at $Re_c = 1.95 \times 10^6$, using three turbulence models: (a) $k-\omega$ SST, (b) Spalart Allmaras (SA), and (c) LS $k-\varepsilon$.

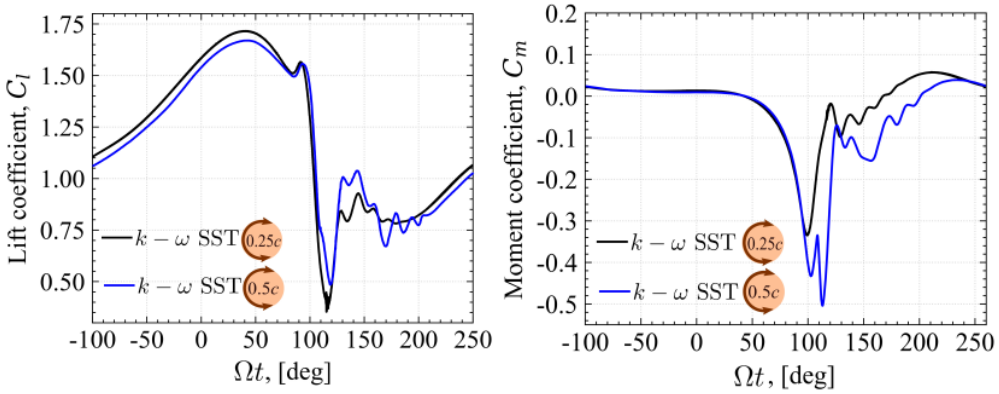

(a) (b)

Fig. 9. Comparison of the lift coefficient and the pitching moment at $x/c = 25\%$, and $x/c = 50\%$ pitching locations (a) Lift coefficients. (b) pitching moment coefficients. Both moments coefficients are computed at the quarter chord point.

As the AoA increases further, the flow reversal that initiates from the trailing-edge can be observed and spreads upstream (see $\alpha \approx 19.49°\uparrow$) with the emergence of a secondary clockwise vortex at the trailing-edge ($\alpha \approx 21.96°\uparrow$). The separation reaches its maximum at $\alpha \approx 22°$ before the airfoil reverses the pitching cycle. However, in contrast to the $k-\omega$ SST, the separation doesn't reach the leading-edge. Moreover, The SA model fails to predict the detachment of the primary counterclockwise vortex within the separated flow region on the suction surface of the airfoil. It should be noted that the lift slope computed by the SA model (Fig. 6b) is lower than the lift slope computed by $k-\omega$ SST (Fig. 6a). Conversely, the drag coefficient is higher. This is attributed to the slightly earlier separation observed than is predicted with the $k-\omega$ SST model (see $\alpha \approx 18.75°\uparrow$). As the airfoil continues to pitch down, the flow reattaches smoothly without inducing severe vortical structures as is the case in the post-stall phase predicted by the $k-\omega$ SST model (see, $\alpha \approx 18.24°\downarrow$ and $\alpha \approx 16.50°\downarrow$ for comparison). This behavior results in a smooth variation of the aerodynamic coefficients (Fig. 6b, Fig. 6e, and Fig. 6h).

4.2.5 The LS $k-\varepsilon$ Model

The computed flow employing the LS $k-\varepsilon$ model is shown in Fig. 8c in terms of the spanwise vorticity contours. In contrast to $k-\omega$ SST and SA models, the LS $k-\varepsilon$ model predicts only a mild separation of the flow on the suction surface of the airfoil in most of the up-stroke motion, namely $\alpha > 18.75°$. The separation region that starts at the trailing-edge spans roughly 50% of the airfoil at the maximum AoA of the oscillating cycle, $\alpha = 22°$. Afterward, as the AoA decreases during the downstroke cycle, the boundary layer reattachment is relatively faster compared to the SA model, as can be seen at AoAs from $\alpha = 22°$ down to $\alpha \approx 14.32°\downarrow$. As a result of this mild separation, the lift curve remains relatively high during the downstroke cycle, and conversely, the drag is low. Additionally, the pitching moment coefficient remains approximately constant, indicating that the center of pressure position is mildly affected.

4.3 Influence of the Pitching Axis Location

In this section, the effects of moving the oscillation axis location downstream at mid-chord ($x/c = 50\%$) are presented. The $k-\omega$ SST model is used, given that it presents a qualitatively good prediction of the unsteady flow compared to the SA and LS $k-\varepsilon$ models. The Lift coefficient and pitching moment coefficient are plotted as a function of the phase angle, Ωt, and shown in Fig. 9a and Fig. 9b, respectively. The results obtained at the quarter-chord ($x/c = 25\%$) are included for comparison as well. Figure 9a suggests that moving the oscillation axis downstream (at mid-chord of the airfoil) results in a reduction in the lift during the upstroke motion compared to the quarter-chord location. This behavior is likely due to the decrease in the effective angle of attack and the relative velocity at the leading-edge and trailing-edge of the airfoil by the aft displacement of the axis (Visbal and Shang 1989). No much difference is observed in the quarter-chord pitching moment, C_m, before stall (see Fig. 9b) for both locations (i.e., $x/c = 25\%$, and $x/c = 50\%$). During the downstroke motion, the lift curve of the airfoil oscillating about its mid-chord exhibits relatively more significant oscillations. Additionally, the airfoil oscillating about $x/c = 50\%$ displays a significant overshoot in the nose-down pitching moment ($C_m \approx -0.5$). Figure 10 illustrates a comparison between the flow development events past the airfoil oscillating about $x/c = 25\%$ and $x/c = 50\%$ in terms of the spanwise component of the vorticity field. During the upstroke phase, namely $12° \leq \alpha \leq 22°\uparrow$, the flow has similar patterns in both cases. However, it is observed that the flow reversal near the trailing-edge is slightly delayed when the airfoil is oscillating about its mid-chord location (see, $\alpha = 18.75°\uparrow$ and $\alpha = 19.49°\uparrow$).

This can also be seen at $\alpha = 22°$ in terms of the formation of DSV. As the airfoil pitches down, despite the delay in the formation of the DSV, the primary flow features characteristics of the post-stall phase are qualitatively similar, i.e., vortical structures over the airfoil's suction surface and their subsequent shedding in the wake.

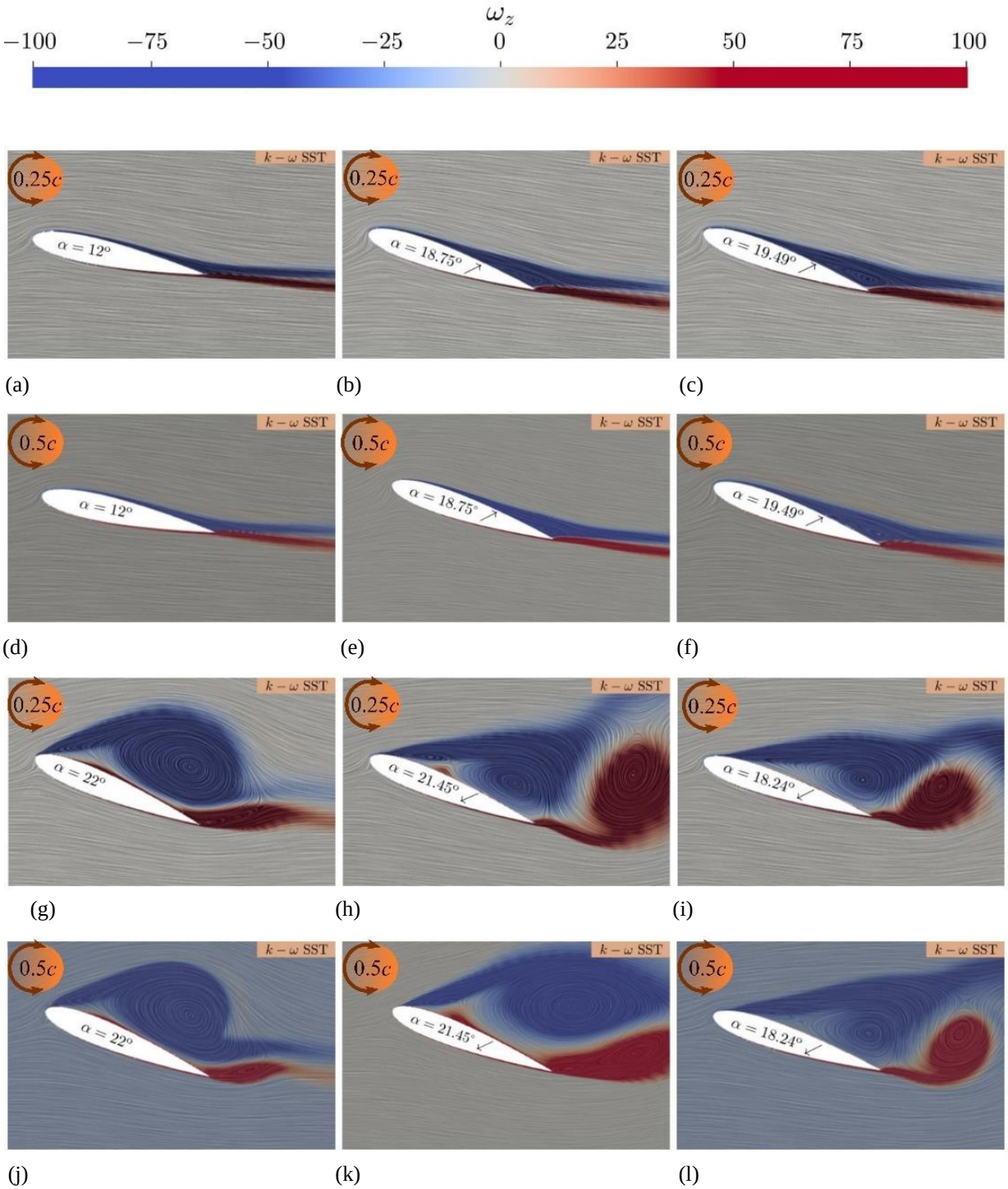

Fig. 10. Vorticity contours of NACA 0015 airfoil oscillating about $x/c = 25\%$ and $x/c = 50\%$ axes at $Re_c = 1.95 \times 10^6$, $\kappa = 0.1$ using the $k-\omega$ SST model. (a)-(l): Comparison at angles: $12°, 18.75°$ ↗, $19.49°$ ↗ , $22°, 21, 45°$ ↙, and $18.24°$ ↙.

5. CONCLUSION

In the present study, URANS computations were carried out incorporating three eddy viscosity turbulence models, namely the Spalart-Allmaras, LS $k-\varepsilon$, and $k-\omega$ SST models using OpenFOAM package to investigate the unsteady turbulent flow around a NACA 0015 airfoil executing a sinusoidal pitching motion about its quarter-chord axis, at chord Reynolds number of 1.95×10^6, and a reduced frequency of 0.1. The airfoil exhibits deep stall under these conditions. Moreover, a series of steady-state simulations have been performed also to predict the static stall. The impact of the pitching axis location, namely at $x/c = 25\%$ and $x/c = 50\%$, has also been investigated. The results of the unsteady simulations have been compared with the experimental data with a tripped flow at the airfoil leading-edge carried out in AMES 7 by 10 wind tunnel of Aeroflightdynamics Directorate (AFDD) at NASA Ames Research Center. In the case of

steady-state simulations with the $k-\omega$ SST turbulence model, it was found that the computed aerodynamic forces and the quarter-chord pitching moment were in good agreement with the experimental data below stall. But for high AoAs, the simulations predict a delay in the static-stall occurrence, hence stall angle is noticeably overpredicted. The results of the unsteady flow simulations involving deep stall over the oscillating airfoil about quarter-chord axis show that the $k-\omega$ SST model performed best among the tested models in terms of predicting the hysteresis loops of the aerodynamic forces and the nose-down pitching moment and the complex flow development. The Spalart-Allmaras and LS $k-\varepsilon$ models fail to predict the deep stall characteristics and yield less separation. It was also found that the $k-\omega$ SST model correctly predicted the mechanism of dynamic stall onset and suggests that the NACA 0015 airfoil exhibits trailing-edge stall. The simulations using the $k-\omega$ SST model of the flow past the airfoil oscillating about the mid-chord axis show that moving the pitching axis location downstream at the mid-chord of the airfoil results in a delay in the onset of dynamic stall and reducing the maximum lift compared to the $x/c = 25\%$. It also has the effect of inducing large overshoot in quarter-chord nose-down pitching moment. However, after dynamic stall occurrence, the primary flow patterns remain similar and are characterized by vortex shedding. Even though this study is limited to fully turbulent unsteady flow, it is believed that in cases involving laminar-turbulence transition, a $k-\omega$ based model such as transition SST $k-\omega$ models would perform better than Spalart-Allmaras and $k-\varepsilon$ family models. Large-eddy simulations would also provide more accurate predictions, particularly in the post-stall phase. This might constitute another topic for future works.

ACKNOWLEDGEMENTS

The authors would like to thank the Directorate General for Scientific Research and Technological Development (DGSRDT) of Algerian government for the research grant to Professor Arezki Smaili and the Natural Sciences and Engineering Research Council (NSERC) of Canada (RGPIN2016-03995) for the research grant to Professor Hachimi Fellouah. Simulations have been carried out using the HPC facilities of the Calcul Québec and Compute Canada networks, which are here also gratefully acknowledged.

CONFLICT OF INTEREST

The authors declare that they have no known competing financial interests or personal relationships that could have appeared to influence the work reported in this paper.

AUTHORS CONTRIBUTION

Samir Ouchene: Conceptualization, Investigation, Methodology, Writing - original draft, Writing; Arezki Smaili: Conceptualization, Funding acquisition, Methodology, Supervision, Review & editing; Hachimi Fellouah: Supervision, Formal analysis, Review & editing, Funding acquisition, Resources.

REFERENCES

Abbas, A., Razak, N., & Zorkipli, M. (2021). Aeroelastic simulation of stall flutter undergoing high and low amplitude limit cycle oscillations. *Journal of Applied Fluid Mechanics*, 14(6), 1679–1689. https://doi.org/10.47176/JAFM.14.06.32439

ANSYS, Inc. (2022). ANSYS Fluent Theory Guide (Version 2022 R1). Canonsburg, PA: ANSYS, Inc.

Bangga, G., & Sasongko, H. (2017). Dynamic stall prediction of a pitching airfoil using an adjusted two-equation URANS turbulence model. *Journal of Applied Fluid Mechanics*, 10(1), 1–10. https://doi.org/10.18869/ACADPUB.JAFM.73.238.26391

Beaudet, L. (2014). *Etude expérimentale et numérique du décrochage dynamique sur une éolienne à axe vertical de forte solidité*. [PhD thesis]. Universite de Poitiers.

Belkheir, N., Dizene, R., & Khelladi, S. (2012). A numerical simulation of turbulence flow around a blade profile of HAWT rotor in moving pulse. *Journal of Applied Fluid Mechanics*, 5(01). https://doi.org/10.36884/JAFM.5.01.11953

Bos, F. M., van Oudheusden, B. W., & Bijl, H. (2013). Radial basis function based mesh deformation applied to simulation of flow around flapping wings. *Computers & Fluids*,79, 167–177. https://doi.org/10.1016/j.compfluid.2013.02.004

Carr, L. W., McAlister, K. W., & McCroskey, W. J. (1977). *Analysis of the development of dynamic stall based on oscillating airfoil experiments*. NASA TN-8382.

Catris, S., & Aupoix, B. (2000). Density corrections for turbulence models. *Aerospace Science and Technology*, 4(1), 1–11. https://doi.org/10.1016/S1270-9638(00)00112-7

Chan, W. M., & Steger, J. L. (1992). Enhancements of a three-dimensional hyperbolic grid generation scheme. *Applied Mathematics and Computation*, 51(2-3), 181–205. https://doi.org/10.1016/0096-3003(92)90073-A

Chitsomboon, T., & Thamthae, C. (2011). *Adjustment of k-ω SST turbulence model for an improved prediction of stalls on wind turbine blades.* World renewable energy congress.

Coleman, D. G., Thomas, F. O., Gordeyev, S., & Corke, T. C. (2019). Parametric modal decomposition of dynamic stall. *American Institute of Aeronautics and Astronautics Journal* 57(1), 176–190. https://doi.org/10.2514/1.J057077

Ekaterinaris, J. A., & Platzer, M. F. (1998). Computational prediction of airfoil dynamic stall. *Progress in Aerospace Sciences*, 33(11-12), 759-846. https://doi.org/10.1016/S0376-0421

Geng, F., Kalkman, I., Suiker, A., & Blocken, B. (2018). Sensitivity analysis of airfoil aerodynamics during pitching motion at a Reynolds number of 1.35×105. *Journal of Wind Engineering and Industrial Aerodynamics*, 183, 315-332. https://doi.org/10.1016/j.jweia.2018.11.009

Gharali, K., & Johnson, D. A. (2013). Dynamic stall simulation of a pitching airfoil under unsteady freestream velocity. *Journal of Fluids and Structures*, 42, 228-244. https://doi.org/10.1016/j.jfluidstructs.2013.05.005

Gharali, K., Gharaei, E., Soltani, M., & Raahemifar, K. (2018). Reduced frequency effects on combined oscillations, angle of attack and free stream oscillations, for a wind turbine blade element. *Renewable Energy*, 115, 252-259. https://doi.org/10.1016/j.renene.2017.08.042

Greenshields, C., & Weller, H. (2022). *Notes on computational fluid dynamics: General principles*. Reading, UK: CFD Direct Ltd.

Gupta, R., & Ansell, P. J. (2018). *Investigation of the effects of Reynolds number on the unsteady flow physics of airfoil dynamic stall*. 2018 AIAA Aerospace Sciences Meeting. American Institute of Aeronautics and Astronautics.

Hand, B., Kelly, G., & Cashman, A. (2021). Aerodynamic design and performance parameters of a lift-type vertical axis wind turbine: A comprehensive review. *Renewable and Sustainable Energy Reviews*, 139, 110699. https://doi.org/10.1016/j.rser.2020.110699

Jasak, H. (2009). Dynamic mesh handling in OpenFOAM. *The AIAA aerospace sciences meeting including the new horizons forum and aerospace exposition*.

Jensen, B. L., Sumer, B. M., & Fredsøe, J. (1989). Turbulent oscillatory boundary layers at high Reynolds numbers. *Journal of Fluid Mechanics*, 206, 265–297. https://doi.org/10.1017/S002211208900230

Kaptein, S. J., Duran-Matute, M., Roman, F., Armenio, V., & Clercx, H. J. (2020). Existence and properties of the logarithmic layer in oscillating flows. *Journal of Hydraulic Research*, 58(4), 687–700. https://doi.org/10.1080/00221686.2019.1661293

Kim, Y., & Xie, Z. T. (2016). Modelling the effect of freestream turbulence on dynamic stall of wind turbine blades. *Computers & Fluids*, 129, 53–66. https://doi.org/10.1016/j.compfluid.2016.02.004

Ko, S., & McCroskey, W. J. (1997). Computations of unsteady separating flows over an oscillating airfoil. *American Institute of Aeronautics and Astronautics Journal*. 35(7), 1235– 1238. https://doi.org/10.2514/2.226

Launder, B., & Sharma B. I. (1974). Application of the energy-dissipation model of flow near a spinning disc. *Letters in Heat and Mass Transfer*, 1(2), 131-137. https://doi.org/10.1016/0094-4548(74)90150-7

Lee, T., & Gerontakos, P. (2004). Investigation of flow over an oscillating airfoil. *Journal of Fluid Mechanics*, 512, 313-341. https://doi.org/10.1017/S0022112004009851

Lee, T., & Su, Y. Y. (2015). Surface pressures developed on an airfoil undergoing heaving and pitching motion. *Journal of Fluids Engineering*, 137(5). https://doi.org/10.1115/1.4029443

Leishman, G. J. (2006). *Principles of helicopter aerodynamics with CD extra*. Cambridge university press.

Leishman, J. G., & Beddoes, T. S. (1989). A Semi-Empirical model for dynamic stall. *Journal of the American Helicopter society*, 34(3), 3-17. https://doi.org/10.4050/JAHS.34.3.3

Li, X., Feng, L. H., & Li, Z. Y. (2019). Flow mechanism for the effect of pivot point on the aerodynamic characteristics of a pitching airfoil and its manipulation. *Physics of Fluids*, 31(8), 087108. https://doi.org/10.1063/1.5114833

McCroskey, W. J. (1981). *The phenomenon of dynamic stall*. NASA-A-National Aeronautics and Space Administration Moffett Field Ca Ames Research Center 8464.

McCroskey, W. J., McAlister, K. W., Carr, L. W., Pucci, S. L., Lambert, O., & Indergrand, R. F. (1981). Dynamic stall on advanced airfoil sections. *Journal of the American Helicopter Society*, 26(3), 40-50. https://doi.org/10.4050/JAHS.26.3.40

Menter, F. R. (1994). Two-equation eddy-viscosity turbulence models for engineering applications. *American Institute of Aeronautics and Astronautics Journal*, 32(8), 1598-1605. https://doi.org/10.2514/3.12149

Menter, F. R., Kuntz, M., & Langtry, R. (2003). Ten years of industrial experience with the SST turbulence model. *Turbulence, Heat and Mass Transfer*, 4(1), 625–632.

OpenCFD. (2022). OpenFOAM version 2112 user guide. Retrieved from https://www.openfoam.com

Petot, D. (1989). Differential equation modeling of dynamic stall. *La Recherche Aerospatiale* (English Edition), 5, 59–72.

Piziali, R. A. (1994). *2-d and 3-d oscillating wing aerodynamics for a range of angles of attack including stall*. Technical Report, NASA Ames Research Center, Moffett Field, CA, NASA Tech Memo 4632, USAATCOM Technical Report 94-A-011; September 1994.

Rhee, M. (2007). *Evaluation of grid convergence and turbulence model constant changes for the airfoil flow simulation*. The AIAA Aerospace Sciences Meeting and Exhibit.

Rhee, M. J. (2002). A study of dynamic stall vortex development using two-dimensional data from the AFDD oscillating wing experiment. *Ames Research Center*, 7, 2002–21185.

Rumsey, C. L. (2007). Apparent transition behavior of widely-used turbulence models. *International Journal of Heat and Fluid Flow*, 28(6), 1460-1471. https://doi.org/10.1016/j.ijheatfluidflow.2007.04.003

Sangwan, J., Sengupta, T. K., & Suchandra, P. (2017). Investigation of compressibility effects on dynamic stall of pitching airfoil *Physics of Fluids*, 29(7), 076104. https://doi.org/10.1063/1.4995457

Sharma, A., & Visbal, M. (2019). Numerical investigation of the effect of airfoil thickness on onset of dynamic stall. *Journal of Fluid Mechanics*, 870, 870-900. https://doi.org/10.1017/jfm.2019.235

Smith, T. A. & Ventikos, Y. (2019). Boundary layer transition over a foil using direct numerical simulation and large eddy simulation. *Physics of Fluids*, 31(12), 124102. https://doi.org/10.1063/1.5126663

Spalart, P. R., & Rumsey, C. L. (2007). Effective inflow conditions for turbulence models in aerodynamic calculations. *American Institute of Aeronautics and Astronautics Journal*, 45(10), 2544-2553. https://doi.org/10.2514/1.29373

Spalart, P., & Allmaras, S. (1992). A oneequation turbulence model for aerodynamic flows. In 30th aerospace sciences meeting and exhibit (p. 439). https://doi.org/10.2514/6.1992-439

Spentzos, A., Barakos, G., Badcock, K., Richards, B., Wernert, P., Schreck, S., & Raffel, M. (2005). Investigation of three-dimensional dynamic stall using computational fluid dynamics. *Aeronautics and Astronautics Journal*, 43(5), 1023-1033. https://doi.org/10.2514/1.8830

Storms, B. L., Ross, J. C., Heineck, J. T., Walker, S. M., Driver, D. M., Zilliac, G. G., & Bencze, D. P. (2001). *An experimental study of the ground transportation system (GTS) model in the NASA Ames 7-by 10-ft wind tunnel.*

Surekha, RS, D., Khandelwal, A., & Rajasekar, R. (2019). Investigation of flow field in deep dynamic stall over an oscillating NACA 0012 airfoil. *Journal of Applied Fluid Mechanics*, 12(3), 857–863. https://doi.org/10.29252/JAFM.12.03.29532

Suvanjumrat, C. (2017). Comparison of turbulence models for flow past NACA0015 airfoil using OpenFOAM. *Engineering Journal*, 21(3), 207-221. https://doi.org/10.4186/ej.2017.21.3.207

Tahry, S. H. E. (1983). K-Epsilon equation for compressible reciprocating engine flows. *Journal of Energy*, 7(4), 345-353. https://doi.org/10.2514/3.48086

Tarzanin, F. J. (1972). Prediction of control loads due to blade stall. *Journal of the American Helicopter Society*, 17(2), 33-46. https://doi.org/10.4050/JAHS.17.33

Thakor, M., Kumar, G., Das, D., & De, A. (2020). Investigation of asymmetrically pitching airfoil at high reduced frequency. *Physics of Fluids*, 32(5), 053607. https://doi.org/10.1063/5.0006659

Tseng, C. C., & Cheng, Y. E. (2015). Numerical investigations of the vortex interactions for a flow over a pitching foil at different stages. *Journal of fluids and structures*, 58, 291-318. https://doi.org/10.1016/j.jfluidstructs.2015.08.002

Visbal, M. R., & Benton, S. I. (2018). Exploration of high-frequency control of dynamic stall using large-eddy simulations. *Aeronautics and Astronautics Journal*, 56(8), 2974-2991. https://doi.org/10.2514/1.J056720

Visbal, M. R., & Garmann, D. J. (2018). Analysis of dynamic stall on a pitching airfoil using high-fidelity large-eddy simulations. *Aeronautics and Astronautics Journal*, 56(1), 46-63. https://doi.org/10.2514/1.J056108

Visbal, M. R., & Shang, J. S. (1989). Investigation of the flow structure around a rapidly pitching airfoil *Aeronautics and Astronautics Journal*, 27(8), 1044-1051. https://doi.org/10.2514/3.10219

Wang, R., & Xiao, Z. (2020). Transition effects on flow characteristics around a static two-dimensional airfoil. *Physics of Fluids*, 32(3), 035113. https://doi.org/10.1063/1.5144860

Wang, S., Ingham, D. B., Ma, L., Pourkashanian, M., & Tao, Z. (2010). Numerical investigations on dynamic stall of low Reynolds number flow around oscillating airfoils. *Computers & Fluids*, 39(9), 1529–1541. https://doi.org/10.1016/j.co

Wang, S., Ingham, D. B., Ma, L., Pourkashanian, M., & Tao, Z. (2012). Turbulence modeling of deep dynamic stall at relatively low Reynolds number. *Journal of Fluids and Structures*, 33, 191-209. https://doi.org/10.1016/j.jfluidstructs.2012.04.011